Acta Materialia 303 (2026) 121604

Contents lists available at ScienceDirect

Acta Materialia

journal homepage: www.elsevier.com/locate/actamat

Full length article

Redefining plasticity in a cubic intermetallic: Dislocation dynamics in the $CaAl_2$ Laves phase

Martina Freund [a,*], Joshua Spille [b], Pei-Ling Sun [a], Marta Lipińska-Chwałek [c], Joachim Mayer [b,c], Zhuocheng Xie [a,*], Sandra Korte-Kerzel [a,*]

[a] Institut für Metallkunde und Materialphysik, RWTH Aachen University, 52056 Aachen, Germany
[b] Central Facility for Electron Microscopy, RWTH Aachen University, 52056 Aachen, Germany
[c] Ernst Ruska-Centre for Microscopy and Spectroscopy with Electrons, Forschungszentrum Jülich GmbH, 52428 Jülich, Germany

ARTICLE INFO

Dataset link: https://zenodo.org/records/17310990

Keywords:
Topologically close-packed phase
Dislocations
Cross-slip
Transmission electron microscopy
Atomistic simulation

ABSTRACT

In the realm of materials design, understanding and manipulating the behaviour of dislocations — key drivers of plastic deformation — is a cornerstone. However, while dislocations are well-explored in simple crystalline materials, their structure and mechanisms of motion remain largely enigmatic for complex crystals, such as topologically closed-packed phases. This vast class of materials contains many intermetallics ranging from high-temperature structural materials to functional crystals that can act as superconductors, magnets, magneto-caloric or hydrogen storage materials. In all of these applications, structural integrity and therefore controlled plasticity is essential. This study bridges our current knowledge gap in plasticity of complex crystals by delving into the most prevalent among them, the Laves phase. Utilizing transmission electron microscopy, we unveil previously unreported defect structures in the cubic $CaAl_2$ Laves phase. Complementing these observations, atomistic simulations elucidate the underpinning mechanisms, revealing novel deformation behaviours. We spotlight the role of full dislocations traversing multiple {1 1 n} slip planes, a departure from the conventional confinement to {1 1 1} planes. This multi-plane dislocation activity, including frequent cross-slipping, emerges as a pivotal factor in accommodating plastic deformation. Our findings not only challenge an existing paradigm in intermetallic plasticity but also propose a tangible pathway to understand the ductility of brittle complex alloys as a stride forward in phase selection and materials engineering.

1. Introduction

Understanding the fundamental principles of plastic deformation of crystals has been and is instrumental in enabling and driving alloy design, as showcased in the explosion of metallic engineering alloys since the first decades of the last century [1]. Current high-performance alloys for structural applications are carefully tailored at multiple length scales from the alloying elements that may distort the metal's lattice at the atomic scale over the local structure at lattice defects imparting strength or deformability, to the interplay of different grains and phases ranging from the nanoscale to the size of metallic sheets. In all but a few exceptions, a single metallic element sits at the heart of a given alloy, e.g. iron in steel, nickel in superalloys or aluminium, titanium or magnesium in the lightweight alloys. In contrast to these alloys centred around the simple cubic and hexagonal unit cells of the parent metal, alloying of comparable amounts of different metallic elements results in the formation of more complex crystalline packings in all but the rare cases where the elements are fully miscible. A vast class of crystals emerges — intermetallics — containing 40,000 [2] reported crystals to date and counting [3]. Even where their formation can be initially suppressed, such as in bulk metallic glasses or high entropy alloys, these phases remain as the thermodynamically stable constituents of most highly alloyed materials. Why then, are they most often considered as phases to be avoided or phases to be constrained to small precipitate sizes in structural alloys? The reason is that most of these crystals are, as a result of their crystal packing, very brittle. However, there are remarkable exceptions with crystals exhibiting plastic deformation at room temperature sufficient for machining or sustaining mechanical impact [4,5]. Given their sheer number and variability, there are bound to be more and exciting intermetallic materials to be found, e.g. for high-temperature structural materials or to enable functions such as superconductivity, magnetism or hydrogen storage in combination with structural integrity and formability. To go in search of these new materials within our existing and expanding material databases or to

* Corresponding authors.
E-mail addresses: freund@imm.rwth-aachen.de (M. Freund), xie@imm.rwth-aachen.de (Z. Xie), korte-kerzel@imm.rwth-aachen.de (S. Korte-Kerzel).

https://doi.org/10.1016/j.actamat.2025.121604
Received 27 March 2025; Received in revised form 3 September 2025; Accepted 29 September 2025
Available online 24 October 2025

purposefully engineer the properties of others, we require the same basic tools as for their simpler metallic cousins: a detailed understanding of how and when dislocations, the key enablers of plastic deformation, move.

Intermetallics have been recognized as an important and attractive class of crystals for a long time and their structures are well described [6]. Topologically close-packed (TCP) structures tend to form when metal atoms of different sizes combine and their ordered and dense atomic packing yields unique properties, such as high melting points, high hardness, elevated corrosion resistance and in many cases also attractive functional properties. However, the high hardness most often comes at the prize of brittleness below the brittle to ductile transition temperature (BDTT), which for these often high-melting crystals is often several hundred Kelvin above ambient conditions. For this reason, previous scientific studies have mostly focused on high-temperature deformation [7–13], or were confined to grown-in and not necessarily mobile defects [14]. Consequently, the dislocation mechanisms are only very poorly understood, particularly in the view of the complex mechanisms of motion encountered in these phases compared with metals. Zonal glide across two parallel planes has been reported in different complex crystals [15–17], while the term 'metadislocations' has been coined for the large cores found in quasi-crystals and their approximants [18–20]. A prominent example of a mechanism unique to complex crystals is synchroshear, a synchronized movement of partial dislocations moving in different parallel planes creating a change in stacking [15]. Originally suggested for sapphire [15], this mechanism was also postulated for the characteristic triple layer of the TCP Laves phases [21,22] and the first high-resolution micrographs of dislocation cores consistent with this mechanism in a hexagonal Laves phase published in 2005 [14], albeit using crystals that were not subjected to plastic deformation. Since then, evidence of synchroshear has been found in other TCP crystals, such as the other Laves phases polytypes, μ-phases or the $CaCu_5$ structure type and computational studies complement the growing body of experimental evidence [23–28]. However, this complex, non-planar mechanism requires thermal activation to take place [26,29] and naturally competes with other mechanisms. It also defies the common expectation of slip taking place on the most close-packed as well as widely spaced set of planes in a crystal [30]. Indeed, it has been shown that the active mechanism of motion in a complex crystal, e.g. crystallographic full or partial dislocation slip or motion of synchro-partials, may be directly manipulated based on small changes in the composition of the alloy, particularly where the crystalline sub-lattice order is affected. This was accompanied by a massive change in yield stress, enabling significant plastic deformation in those layers with Laves phase packing in larger but closely related μ-phase structure [4,5]. In hexagonal Laves and the similarly structured μ-phases, dislocations have also been found to move on non-basal planes [31–36], that is outside of the triple layer. Conversely, for the cubic Laves phases, plasticity had been reported to take place exclusively on the {1 1 1} planes, which contain the characteristic triple layer equivalent to the basal plane in the hexagonal polytypes. It is only very recently that the first experimental evidence suggested that deformation may take place outside of the {1 1 1} plane in cubic Laves phases, in contrast to what is observed in the much simpler face-centred cubic metals [37].

To unravel the active mechanisms of motion in this large and technologically important class of TCP Laves phases and their crystallographic relatives, we address here a fundamental question: which dislocation mechanisms are active in the cubic Laves phases and how can they be understood and related to previous insights restricted to high-temperature behaviour?

2. Methods

2.1. Sample preparation

Binary $CaAl_2$ Laves phases, which belong to the space group 227 ($[Fd\bar{3}m]$ and Pearson Symbol cF24), were prepared like described in [38]. Further ternary C15 $Ca(Al,Mg)_2$ Laves phases were embedded in a copper paste to reveal a stable sample surface. Laves phase samples were prepared metallographically, by using four grinding steps using SiC paper with a grit site of 1200 to 4000, whereas for the ternary additional grinding steps using diamond grinding plates (POLARIS M) with grain sizes of 6 μm and 3 μm, followed by mechanical polishing with diamond paste starting with 6 μm and ending with 0.25 μm using for all steps isopropanol with 5% polyethylene glycol 400 (PEG) as lubricant. Final polishing and washing steps were followed with a grain size of 0.04 μm (using STRUERS OPA) and cleaning with dish washing liquid. Both samples were analysed using scanning electron microscopy (SEM) (CLARA, Tescan, Brno, Czech Republic), energy dispersive X-ray spectroscopy (EDX) (Helios Nanolab 600i, FEI, Eindhoven, NL) and additional electron backscatter diffraction (EBSD) (Helios Nanolab 600i, FEI, Eindhoven, NL) to analyse the resulting microstructure and the resulting plastic zone, the local chemical composition and the grain orientations.

2.2. Nanoindentation experiments

To investigate the mechanical properties and resulting plasticity, nanomechanical tests were performed using an iNano nanoindenter (Nanomechanics Inc., TN, USA) with a diamond Berkovich tip (supplied by Synton-MDP AG, Switzerland). The Oliver and Pharr method was used to calibrate the setup on a fused silica sample by determining the diamond area function (DAF) and frame stiffness of the indenter tip [39,40] The indents were performed with the same parameters, using a constant strain rate of 0.2 s^{-1} until a depth of 500 nm was reached. The analysis included the evaluation of the indentation modulus, hardness, and activated slip systems by aligning surface traces from the SE images with grain orientation from the EBSD analysis, as described in the review by Gibson et al. [41].

2.3. TEM characterization

Individual slip bands beneath the surface were analysed in a Jeol JEM F200 TEM at 200 kV. This microscope is equipped with a double-tilt holder, in which x-tilting of ±36° and y-tilting of ±31° are allowed. Scanning transmission electron microscopy (STEM) was also performed with the same application. Additionally, higher resolution STEM analysis of the binary and ternary $CaAl_2$ Laves phases was performed on an aberration corrected FEI Tian 60-200 ChemiSTEM at 200 kV acceleration voltage. Site specific TEM lamella were taken out by ion milling in FIB. The lamellae were tilted to different zone axes and several two-beam conditions in order to identify edge-on orientation of the possible slip planes and confirm the corresponding habit planes of the dislocation slip [42]. DPs of the zone axes and two-beam condition (bright/dark-field) images of the investigated defects were acquired.

2.4. Atomistic simulations

Atomistic simulations were performed using the open-source molecular dynamics code LAMMPS [43]. The interatomic interactions were modelled employing the machine-learning moment tensor potential (MTP) by Poul et al. [37,44] for the Al-Ca system. The machine-learning MTP potential provides better predictions in lattice parameter, elastic constants and {1 1 1} stacking fault energy compared to the semi-empirical modified embedded atom method (MEAM) potential [45] when compared with ab-initio and experimental results [37].

The C15 $CaAl_2$ crystal structures were constructed using Atomsk [46]. A screw full dislocation with a Burgers vector of $\frac{a}{2}[\bar{1}\,1\,0]$ was introduced on different glide planes following the method detailed in [25]. Periodic boundary conditions (PBCs) were applied in the directions along the glide plane, while semi-fixed boundary conditions were applied in the normal direction to the glide plane. The simulation setups are illustrated in Fig. 1(a). The atomistic configurations were relaxed ug

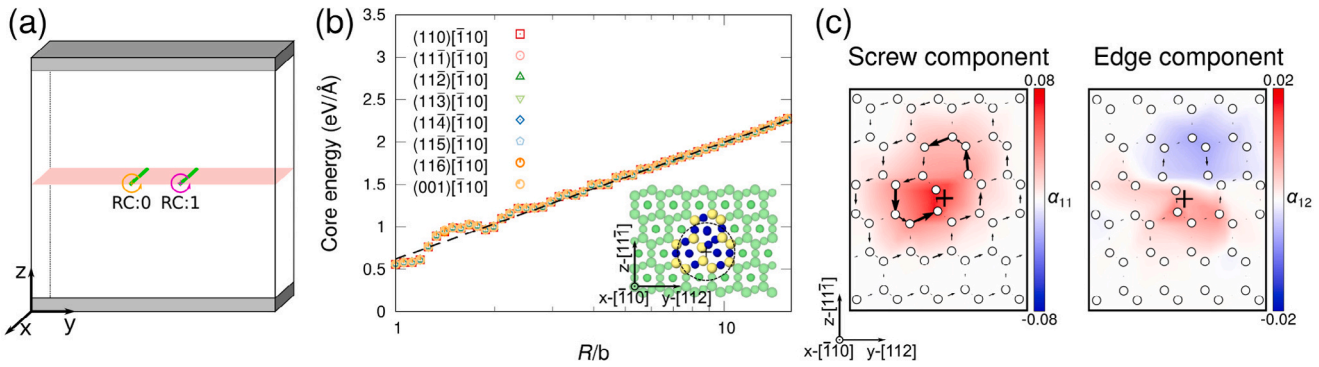

Fig. 1. (a) Schematic illustration of the simulation setup for dislocation motion. Climbing image NEB calculations were performed on the initial (RC:0) and final (RC:1) configurations to find MEPs for dislocation motion. PBCs were applied in the x ($[\bar{1}10]$-oriented) and y directions. Atoms in the outermost layers (marked in grey) with a thickness of 15 Å(2 times the potential cut-off) were fixed in the z-direction. The dimensions of the setup in the y and z directions are 200 Å, and in the x direction, it is 11.3 Å. The dislocation line and Burgers vector of screw $\frac{a}{2}[\bar{1}10]$ dislocations are along the x-direction, and the glide distance is one unit length along the y-direction. (b) Core structure and energy of the screw $\frac{a}{2}[\bar{1}10]$ dislocation in the simulated $CaAl_2$ Laves phase. Only atoms belonging to the dislocation core, as identified by LaCA, are highlighted (Ca and Al atoms are coloured in yellow and blue, respectively) here. (c) Nye-tensor and differential displacement maps of the screw $\frac{a}{2}[\bar{1}10]$ dislocation in the Ca sublattice. (For interpretation of the references to colour in this figure legend, the reader is referred to the web version of this article.)

the conjugated gradient algorithm with box relaxation and the FIRE algorithm [47,48], with a force threshold of 10^{-8} eV/Å. The dislocation core energy was calculated by measuring the total dislocation energy as a function of radius R and then extrapolating the far-field elastic energy back to the chosen cut-off radius b, as shown in Fig. 1(b).

Climbing image nudged elastic band (NEB) calculations [49,50] were performed on the initial (before dislocation glide) and final (after dislocation glide) configurations to determine the minimum energy paths (MEPs) for these dislocation motion events (see Fig. 1(a)). The spring constants for parallel and perpendicular nudging forces are both 1.0 eV/Å^2. The QUICKMIN algorithm [51] was applied as the damped dynamics minimizer for energy minimization with a force threshold of 10^{-2} eV/Å. The number of intermediate replicas ranged from 96 to 312, depending on the glide distance and corresponding dissociation events. Laves phase crystal analysis (LaCA) [52] was used to identify dislocation cores in C15 Laves phases and dislocation analysis (DXA) [53] implemented in OVITO [54] was used to extract dislocation lines.

3. Results

3.1. Slip beyond {1 1 1} planes

Nanoindentation was used to introduce plastic deformation in different orientations of a poly-crystalline $CaAl_2$ C15 Laves phase, giving rise to significant deformation on different crystallographic planes as seen on the surface around an indentation impression for $CaAl_2$ (Fig. 2(a)) and $CaAl_2$ + Mg (Fig. 3(a)). Several active slip planes were found. The straight ones can directly be assigned to specific planes, like shown for the $CaAl_2$ in (Fig. 2(a)), while some of them are wavy and cannot be directly assigned to a specific slip plane (Fig. 2(a)). Additionally, three cracks formed along the three corners of the indent for the stoichiometric sample (Fig. 2(a)). Transmission electron microscopy (TEM) on electron transparent lamellae lifted out of the material as a cross-section of such indentations allowed us to further investigate the nature of the underlying crystallographic planes accommodating plasticity. At the sub-micron scale of a diffraction-guided analysis using conventional TEM for the $CaAl_2$ + Mg sample (Fig. 3(b)–(d)), we reveal clear changes in orientation in the slip planes travelling into the material. Additionally, (Fig. 3(b)–(d)) shows that, compared to the planes observed below, the transition between planes can occur in small, alternating segments embedded between the larger straight segments. Examples of slip taking place on {1 1 1}, {1 1 2} and {1 1 5} planes are shown here, with {1 1 3}, {1 1 4}, {1 1 6} and {1 1 11} planes also found elsewhere [37]. Similarly, some of the cracks emerging from or forming along these slip planes also progress in a zigzag pattern, consistent with their preferential formation along slip planes that have accumulated a high density of defects [31]. Dislocation analyses using different two-beam conditions show that in all cases dislocations moving on these planes share the same Burgers vector, which is of $\langle 1\,\bar{1}\,0\rangle$ type. HR-TEM imaging, given in (Fig. 2(b)) for the $CaAl_2$ sample, at the atomic scale using an aberration-corrected scanning transmission electron microscope, reveals that even at the smallest scales, similar changes in slip planes are observed. These are consistent with cross-slip taking place via $\langle 1\,\bar{1}\,0\rangle$ screw dislocations whose Burgers vector is contained in all of the experimentally encountered $\{1\,1\,n\}$ planes. As such, the crystal appears to deform on many more planes than previously reported or anticipated. Furthermore, (Fig. 2(c)) shows a conventional TEM image of the C15 ternary sample, which illustrates the progression of the slip planes along a zigzag path. This is also shown in more detail in Fig. 3((b)–(d)) including an indexation of the individual plane segments imaged on edge. The area marked with a white rectangle in (Fig. 2(c)) is the area recorded in (Fig. 2(d)) using STEM in dark field mode. In the STEM image, the lower feature in particular is contained in an initial plane, followed by a cross-slip to the next plane. This process then repeats (from left to right in the image, corresponding to increasing distance to the centre of the plastic zone) via a plane that is parallel to the initial one and continues parallel to the initial cross-slip plane. Whether crack formation occurs before, during or after this process has completed cannot be derived from these post-mortem images.

3.2. Atomistic simulations of dislocation motion

To unravel the underlying mechanisms of slip, particularly the new observation of frequent cross-slip in the C15 $CaAl_2$ Laves phase attributed to screw dislocation motion, we used atomistic simulations. To this end, we performed NEB calculations using a newly developed machine-learning MTP to determine the MEPs of screw dislocation motion on the different $\{1\,1\,n\}$ planes as well as the low-index $\{1\,0\,0\}$ and $\{1\,1\,0\}$ planes. For both, the known and new slip planes, we identified an identical core of the screw $\frac{a}{2}[\bar{1}\,1\,0]$ dislocation (Fig. 1(b-c)). As shown in Fig. 1(c), the Nye tensor distribution reveals a small but non-negligible edge component at the screw dislocation core region, which is attributed to core spreading along the $(0\,0\,1)$ plane, as confirmed by the corresponding differential displacement map. While the core structure remains unchanged, notable differences emerge during the motion of these dislocations. The transition processes and associated

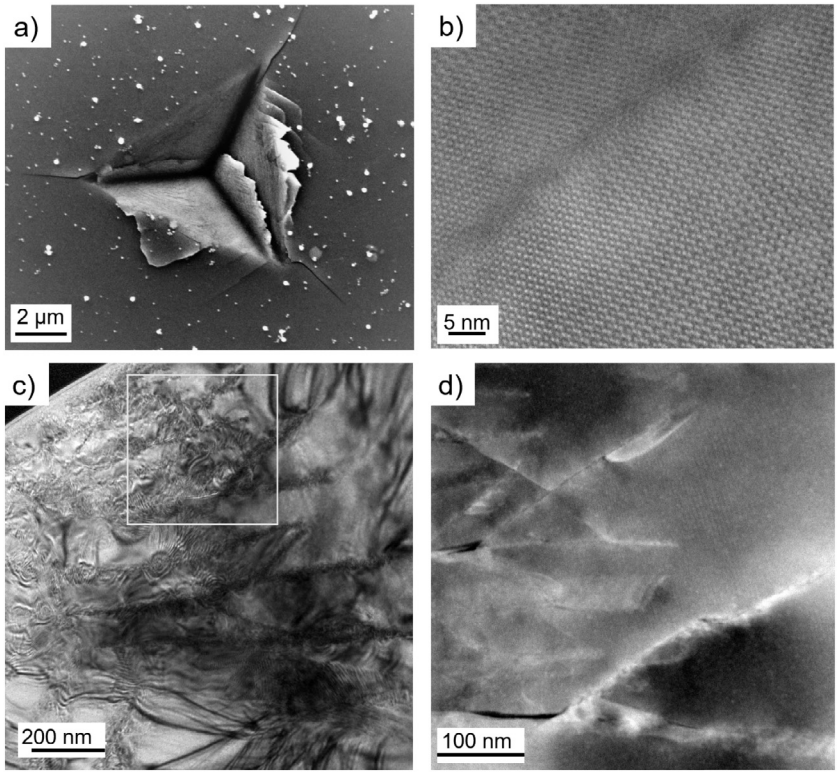

Fig. 2. Deformation structure around an indent imaged by electron microscopy. (a) Secondary electron micrograph of slip traces on the sample surface and (b) HRTEM image recorded in the [1 1 0] zone axis for the binary C15 $CaAl_2$ Laves phase. (c) Conventional and (d) STEM dark field images of the ternary C15 $Ca(Al,Mg)_2$ Laves phase at the [1 1 0] zone axis. The area imaged in (d) is indicated by a white rectangle in (c).

energy barriers of all individual activation events of dislocation movements in this study are summarized in Table 1. For dislocations gliding on (1 1 0), (1 1 $\bar{1}$), and (1 1 $\bar{3}$) planes with glide distances smaller than 10 Å, no intermediate states featuring restored dislocation cores and zero relative energy (ΔE = 0 eV) were found along the MEPs (see Fig. 4). Although atomic movement during glide includes out-of-plane components, as illustrated in Supplementary Movies S1–S4, the overall dislocation motion remains confined to the horizontal glide plane and is thus considered in-plane. For the screw (0 0 1)[$\bar{1}$ 1 0] dislocation, an intermediate configuration with a dislocation core equivalent to the initial state (at RC = 0) and energy ΔE = 0 eV was identified at the RC of 0.5 (see Fig. 5(a) and Movie S5). However, this intermediate core remains confined to the same (0 0 1) glide plane. Among these in-plane slip processes, the screw dislocation on the (1 1 $\bar{1}$) triple-kagome plane exhibits the shortest glide distance of 4.91 Åand the lowest energy barrier of 0.107 eV/Å, which is significantly lower than that of the competing (1 1 $\bar{1}$) triple plane, where the mechanism of motion is dominated by synchro-Shockley partial dislocations, as demonstrated in our previous studies [24,25]. The (1 1 $\bar{3}$)[$\bar{1}$ 1 0] dislocation exhibits both the longest glide distance of 9.39 Åand the highest energy barrier of 0.266 eV/Åamong the in-plane slip processes.

In contrast, for dislocations gliding on (1 1 $\bar{2}$), (1 1 $\bar{4}$), (1 1 $\bar{5}$) and (1 1 $\bar{6}$) planes with glide distances larger than 10 Å, the motion breaks up into movement between different glide planes, accompanied by cross-slip processes along the transition paths (see Fig. 5(b-e) and Movies S6-S9). For instance, the screw dislocation gliding on the (1 1 $\bar{2}$) plane undergoes decomposition into two sub-events: one corresponds to the dislocation gliding on the (1 1 $\bar{3}$) plane, and another one involves the dislocation gliding on the (1 1 $\bar{1}$) plane. These events are separated by an energy minimum (ΔE = 0), corresponding to the dislocation state equivalent to the initial configuration (RC = 0), and accompanied by a cross-slip process. Similarly, the motion of the screw (1 1 $\bar{5}$)[$\bar{1}$ 1 0] dislocation decomposes into gliding along (0 0 1) and (2 2 $\bar{7}$) planes with cross-slip occurring between them. The (2 2 $\bar{7}$)[$\bar{1}$ 1 0] slip exhibits a similar energy profile to the (1 1 $\bar{3}$)[$\bar{1}$ 1 0] slip but with a higher energy barrier. Furthermore, the (2 2 $\bar{7}$) plane is geometrically close to the (1 1 $\bar{3}$) plane, suggesting that the (2 2 $\bar{7}$) slip can be considered a variation of the (1 1 $\bar{3}$) slip, involving a structural transition at the dislocation core. For dislocation movement on the (1 1 $\bar{4}$) plane, in addition to the transitions between (0 0 1) and (2 2 $\bar{7}$) planes as seen in the (1 1 $\bar{5}$)[$\bar{1}$ 1 0] dislocation motion, an additional intermediate local minimum and a cross-slip process from (1 1 $\bar{3}$) to (0 0 1) planes are identified. Slip processes on the (1 1 $\bar{4}$) and (1 1 $\bar{5}$) planes exhibit comparable energy barriers (0.314 and 0.315 eV/Å, respectively), as the (2 2 $\bar{7}$) slip represents the rate-limiting step in both cases. The screw (1 1 $\bar{6}$)[$\bar{1}$ 1 0] dislocation exhibits the longest glide distance (34.90 Å) among all simulated dislocations. Its motion consists of multiple intermediate minima and cross-slip events, as well as extension and constriction of the dislocation core (Fig. 5(e)). Across all simulated screw dislocations, no dissociation into partials bounded by stacking faults was observed along the MEPs.

4. Discussion

Plasticity in Laves phases is clearly much more complex than indicated in previous investigations. Recent advances in experimental and computational methods have allowed us to draw a more complete picture of how plasticity takes place in these most common intermetallic phases [6] and build the foundation that not only connects the different Laves phase polytypes but also enables us to infer and predict deformation mechanisms and mechanical properties of other intermetallic phases that contain the Laves phase as an important building block [5,6].

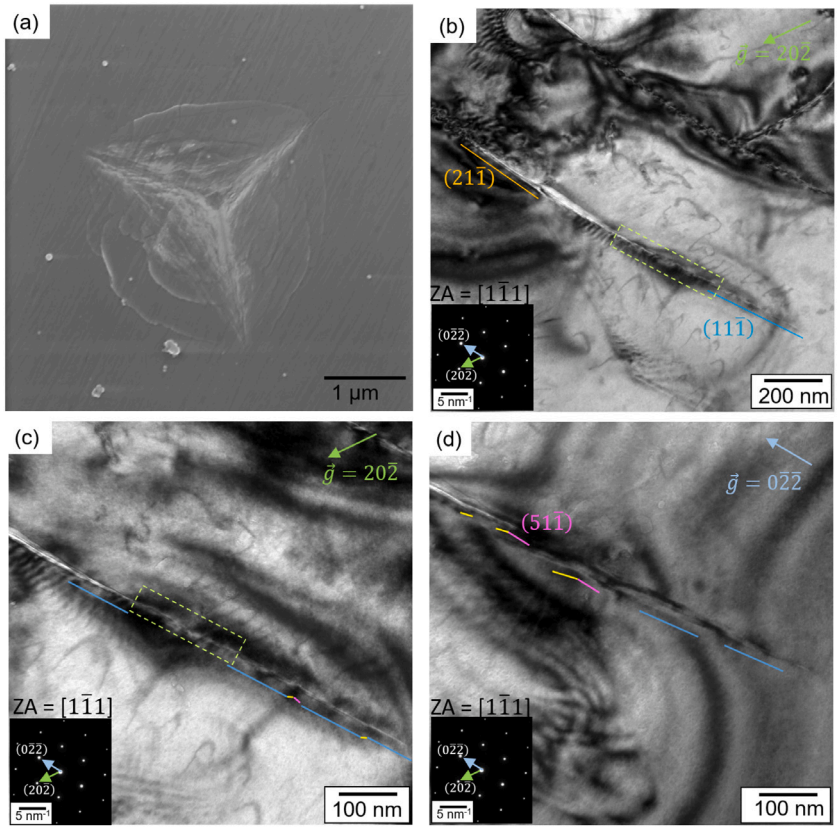

Fig. 3. (a) A SE image showing the slip trace morphology after nanoindentation of the C15 $Ca(Al,Mg)_2$ Laves phase. (b) TEM bright field image taken under $\vec{g} = 0\bar{2}\bar{2}$ in a $\vec{g} = 1\bar{1}1$ zone axis represents the underlying dislocation structure of the in (a) shown indent. The $(2\,1\,\bar{1})$ plane traces are shown with the orange line and the $(1\,1\,\bar{1})$ with the blue one. TEM bright field images taken under (c) the same conditions used in (b) and (d) $\vec{g} = 0\bar{2}\bar{2}$ two-beam conditions at, highlighting the zigzag structure from (c) in (d) shown with the green dashed rectangle. The $(2\,1\,\bar{1})$ and $(1\,1\,\bar{1})$ plane traces are shown next to the crack. The crack is observed to have a zigzag feature. Different colour lines mark the orientations of the slip planes. The green rectangle shows a segment where the crack is quite wavy. (For interpretation of the references to colour in this figure legend, the reader is referred to the web version of this article.)

Table 1
Summary of glide distance, transition process, and associated energy barriers of the screw $\frac{a}{2}[\bar{1}10]$ dislocation motion on different glide planes.

Glide plane	Glide distance (Å)	Transition process	Energy barrier (eV/Å)
(110)	8.01	(110)	0.116
$(11\bar{1})$ triple-kagome	4.91	$(11\bar{1})$	0.107
$(11\bar{1})$ triple	4.91	$(11\bar{1})$	0.160
$(11\bar{2})$	13.87	$(11\bar{3})$ + $(11\bar{1})$	0.284, 0.075
$(11\bar{3})$	9.39	$(11\bar{3})$	0.266
$(11\bar{4})$	24.02	$(11\bar{3})$ + (001) + $(22\bar{7})$	0.267, 0.115, 0.314
$(11\bar{5})$	14.71	(001) + $(22\bar{7})$	0.115, 0.315
$(11\bar{6})$	34.90	(001) + core extension + core constriction + $(22\bar{7})$ + (001) + $(11\bar{6})$	0.114, 0.144, 0.144, 0.367, 0.115, 0.159
(001)	5.66	(001) + (001)	0.076, 0.115

4.1. Atomistic mechanisms of cross-slip in laves phases

One of the central findings of this study is the frequent occurrence of cross-slip between multiple $\{1\,1\,n\}$ planes. This behaviour challenges the conventional view that plasticity in Laves phases is confined to a narrow set of crystallographic planes, particularly $\{1\,1\,1\}$. Instead, our results show that perfect screw dislocations can glide and cross-slip between a variety of planes, enabled by their undissociated core structures. Atomistic simulations confirm that the screw dislocation cores remain compact across all studied slip systems, and no dissociation into partials or formation of stable stacking faults occurs along any of the calculated MEPs. These results are consistent with prior work showing an absence of metastable stacking faults along these slip paths in C15 $CaAl_2$ [37].

Although experimental observations revealed dislocation motion along various $\{1\,1\,n\}$ planes over distances ranging from tens to hundreds of nanometres (see Figs. 2 and 3), the atomistic simulations suggest that these macroscopically observed slip traces are governed by a smaller set of fundamental slip events. Specifically, dislocation glide occurs through elementary motion on the $\{1\,1\,1\}$, $\{1\,1\,3\}$, $\{0\,0\,1\}$, and $\{2\,2\,7\}$ planes. These foundational slip processes exhibit energy barriers comparable to those of individual slip events or as intermediate sub-events within cross-slip transitions (see Table 1). The calculated energy barriers associated with these transitions range from 0.1 to 0.4 eV/Å, in agreement with values reported for other structurally complex crystals. For instance, out-of-plane glide-to-climb transitions in perovskite $SrTiO_3$ exhibit barriers between 0.08 and 0.6 eV/Å, depending on the charge state of the dislocation core [55]. It is worth noting that the dislocations modelled in this study are straight, which

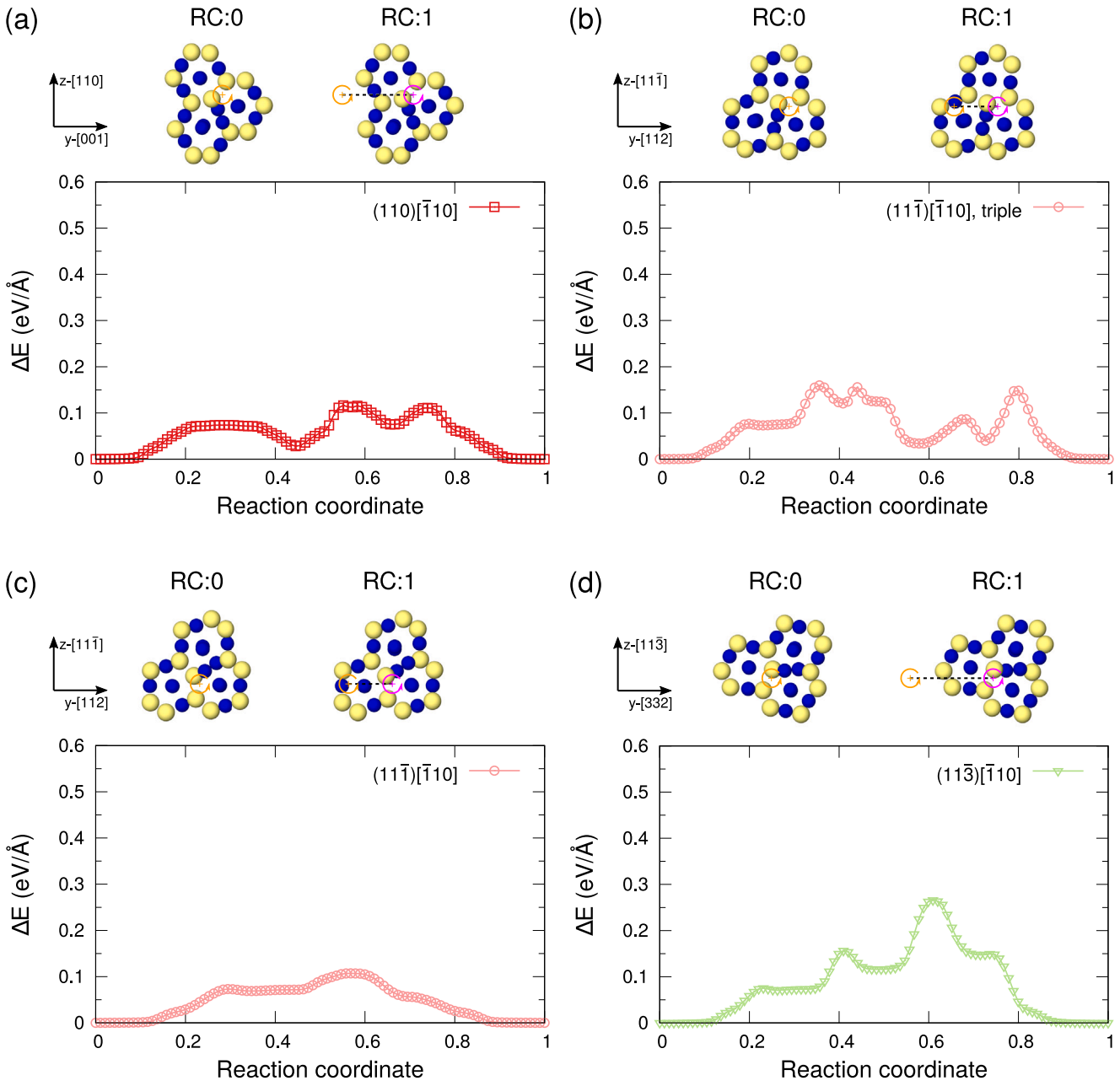

Fig. 4. Atomistic configurations and energy profiles along MEPs for the motion of the screw $\frac{a}{2}[\bar{1}\,1\,0]$ dislocation on (a) (1 1 0), (b) (1 1 $\bar{1}$) triple layer, (c) (1 1 $\bar{1}$) triple-kagome layer, and (d) (1 1 $\bar{3}$) planes in the C15 $CaAl_2$ Laves phase were calculated using the NEB method. Only atoms belonging to the dislocation core are shown here. The orange and magenta symbols indicate the position of the dislocation line in the initial (reaction coordinate RC:0) and final (RC:1) atomistic configurations, while the cyan symbols represent the position of the dislocation line at the intermediate minima. Dashed lines indicate the glide planes between each local minimum. (For interpretation of the references to colour in this figure legend, the reader is referred to the web version of this article.)

results from the limited simulation cell length along the dislocation line direction. This constraint is due to the high computational cost of the moment tensor interatomic potential, which is three orders of magnitude more expensive than classical semi-empirical potentials, like embedded atom method potentials. As a result, the simulations do not capture local dislocation line curvature, such as bowing-out or kink-pair nucleation, which can lower the energy barrier of rate-limiting steps. The reported values here may therefore represent upper bounds for the true activation barriers of these slip events.

Furthermore, the screw dislocation in C15 $CaAl_2$ shows a tendency to spread along the (0 0 1) plane, suggesting that out-of-plane atomic displacements play a significant role in dislocation motion, see Movies S1-9 in the Supplementary Information. Such out-of-plane effects are often associated with non-Schmid behaviour and have previously been reported in synchro-Shockley dislocation motion in Laves phases via atomistic simulations [26]. Similar phenomena have also been observed experimentally in layered crystalline materials such as MAX phases [56, 57]. Nevertheless, to fully understand the role of normal stress components in cross-slip behaviour in Laves phases, further experimental validation, such as through micropillar compression testing, and more extensive atomistic modelling will be essential.

4.2. Temperature-dependent plasticity in laves phases

Nanomechanical testing allowed us to induce plasticity at low temperatures far below the BDTT. In combination with imaging and analysis of numerous indentation imprints at the micron scale and dedicated

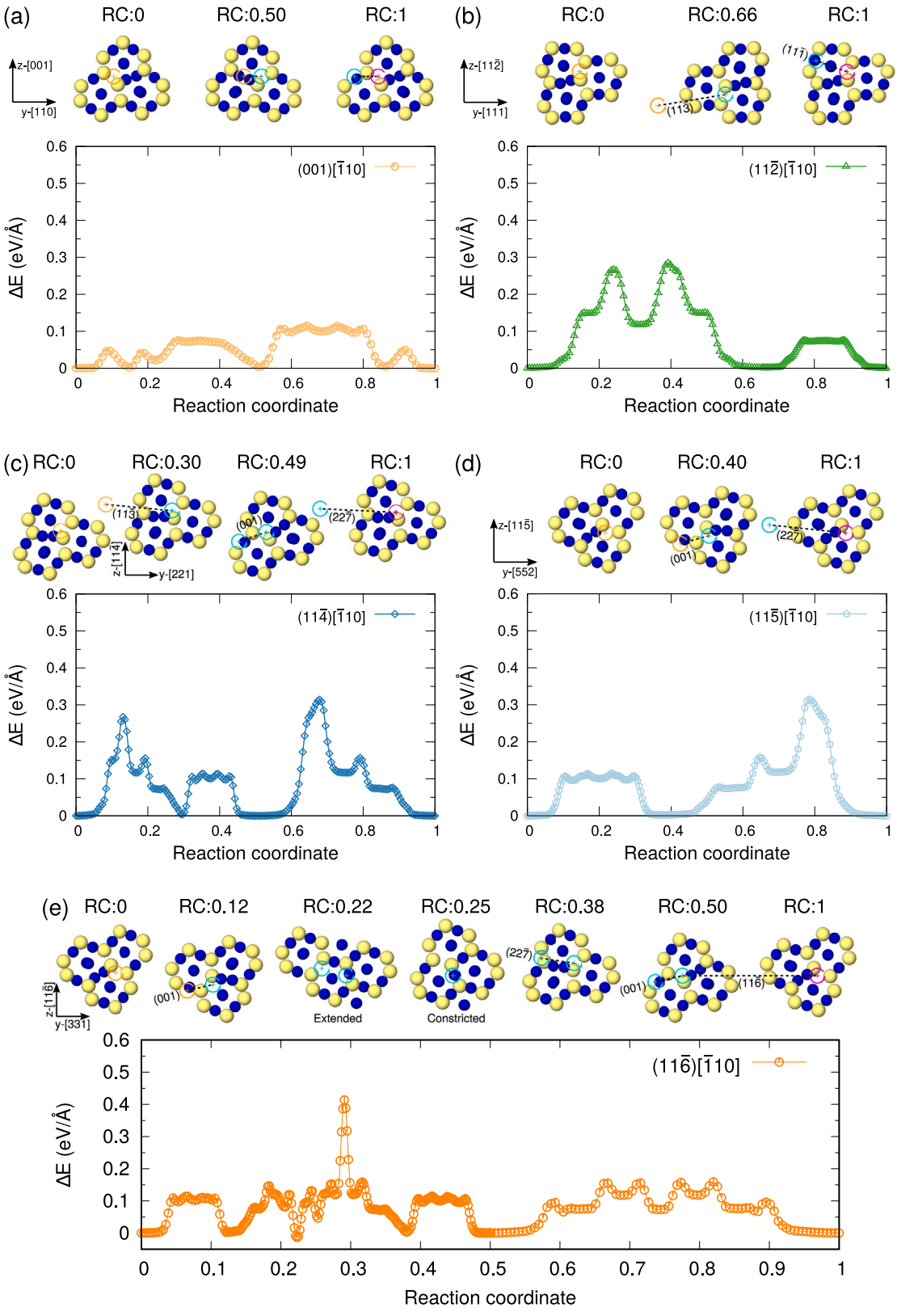

Fig. 5. Atomistic configurations and energy profiles along MEPs for the motion of the screw $\frac{a}{2}[\bar{1}\,1\,0]$ dislocation on (a) (0 0 1), (b) (1 1 $\bar{2}$), (c) (1 1 $\bar{4}$), (d) (1 1 $\bar{5}$), and (e) (1 1 $\bar{6}$) planes in the C15 $CaAl_2$ Laves phase were calculated using the NEB method. Only atoms belonging to the dislocation core are shown here. The orange and magenta symbols indicate the position of the dislocation line in the initial (reaction coordinate RC:0) and final (RC:1) atomistic configurations, while the cyan symbols represent the position of the dislocation line at the intermediate minima. Dashed lines indicate the glide planes between each local minimum. (For interpretation of the references to colour in this figure legend, the reader is referred to the web version of this article.)

defect analysis by TEM, we could reveal that slip planes beyond those previously reported in the literature [13] are active and, in fact, accommodate the majority of plastic deformation. Unravelling that and how dislocations cross-slip between a subset of the macroscopically observed planes by high-resolution microscopy and atomistic modelling gives us the basis to interpret plastic deformation of the Laves phase more generally. For example, the observed cross-slip of $[\bar{1}\,1\,0]$ dislocations on $\{1\,1\,n\}$ planes gives rise to the orientation dependence of deformation evidenced by the changing surface features in indentation [29]. Similarly, uncovering the mechanisms governing dislocation motion is essential to connect observations of mechanical properties and active mechanisms across a range of temperatures and strain rates.

Previous work revealed the thermally activated nature of the synchroshear mechanism [14,15,25,26] and provided a basis on which to understand the occurrence of conventional dislocation motion in parallel $\{1\,1\,1\}$ interlayers of the C15 Laves phase or $(0\,0\,0\,1)$ interlayers in the hexagonal polytypes. It is now apparent that the slip of $\langle 1\,\bar{1}\,0\rangle$ dislocations is what facilitates the manifold of slip planes by allowing cross-slip onto the many available $\{1\,1\,n\}$ planes via a combination of fundamental slip events on $\{1\,1\,1\}$, $\{1\,1\,3\}$, $\{0\,0\,1\}$, and $\{2\,2\,7\}$ planes. This understanding provides a clear path to connect deformation at different temperatures: at low temperatures, glide occurs on planes offering least resistance and the compact dislocation cores of $\langle 1\,\bar{1}\,0\rangle$ dislocations facilitate cross-slip and thereby dislocation motion under maximum resolved shear stress across variable stress fields (as induced in indentation in this work). Previous observations at elevated temperature [13] on the other hand, are consistent with thermal activation favouring slip by synchroshear, confining deformation to only $\{1\,1\,1\}$ planes. As synchroshear operates by the formation and motion of partials on $\{1\,1\,1\}$ planes, this dominance of $\{1\,1\,1\}$ slip at elevated temperatures may be related to thermally activated dislocation dissociation blocking further cross-slip [58], here onto the $\{1\,1\,n\}$ planes on which only the partials cannot glide or cross-slip, thereby depriving the $\{1\,1\,n\}$ planes of mobile dislocations.

Nanoindentation at different temperatures has revealed a near-constant hardness below the brittle to ductile transition [59], but recent work expanding into the regime of dropping critical stresses [60] indicated possible hardening with temperature before the hardness drop associated with the brittle to ductile transition. Whether this is a reproducible and more general feature of deformation of Laves phases owing to the thermally activated dissociation and cross-slip processes, remains to be explored. Transmission electron microscopy investigations of an indentation print deformed at elevated temperatures [29,59,60] enable to confirm this hypothesis or shed light on additional transient mechanisms controlling flow in Laves phases, by finding beside perfect dislocations, which were previously observed at ambient temperature, additionally partial dislocations for high temperature (450 °C). Similarly, experiments and modelling will build on the newly identified fundamental mechanisms of dislocation motion to study the effect of composition on dislocation motion, where the interplay of hardening and softening mechanisms introduced by an excess of either small or large atoms and the resulting formation of anti-site defects and/or vacancies, remains poorly understood.

4.3. Insights into intermetallic design

The ability to understand, predict and tailor plasticity in Laves phases and those crystals with larger unit cells where plasticity takes place predominantly in Laves phase building blocks, will enable materials and process design for a range of applications. For example, the frequent Laves phase precipitates in steels, superalloys or high entropy alloys may be harnessed intentionally in the design process. Controlling Laves polytype or related phases containing Laves phase as a building block in precipitates may enable shifts in mechanical contrast to the matrix phase [5] and mechanisms of hardening or damage formation by blocking or enabling co-deformation via slip system and coherent interface selection [61,62]. In use as functional materials, in particular for hydrogen storage, understanding and purposeful manipulation can be employed at several stages of the processing and use of Laves phase based materials. For example, pronounced brittleness eases powder production, conversely, the introduction of crystal defects and perhaps also selection of the most prevalent defect type, can improve (de)hydrogenation kinetics [63,64]. For both, the ability to manipulate which dislocations form and under which stresses they move is essential and may be achieved by means of altering composition as well as choosing adequate processing conditions with respect to deformation rate and temperature, be it during milling, mechanical alloying or severe plastic deformation.

5. Conclusion

In conclusion, we revealed how deformation in a Laves phase occurs in the low-temperature regime and provide a powerful starting point for a purposeful materials and process design with Laves phases. Importantly, plasticity in this exceedingly common and technologically relevant intermetallic phase is much more versatile than previously expected. Active dislocation mechanisms depend sensitively on thermal activation, increasing our scope as material scientists and engineers to control and use their behaviour and move beyond the simple view of the Laves phase as a purely brittle material to begin to purposefully consider its carriers of plastic deformation.

CRediT authorship contribution statement

Martina Freund: Writing – original draft, Visualization, Investigation, Formal analysis, Conceptualization. **Joshua Spille:** Writing – review & editing, Resources. **Pei-Ling Sun:** Investigation. **Marta Lipińska-Chwałek:** Writing – original draft. **Joachim Mayer:** Supervision. **Zhuocheng Xie:** Writing – original draft, Visualization, Investigation, Conceptualization. **Sandra Korte-Kerzel:** Writing – original draft, Supervision, Conceptualization.

Declaration of competing interest

The authors declare that they have no known competing financial interests or personal relationships that could have appeared to influence the work reported in this paper.

Acknowledgements

The authors gratefully acknowledge financial support by the Deutsche Forschungsgemeinschaft (DFG) to all projects involved in this paper A02, A03, A05 and Z the SFB1394 Structural and Chemical Atomic Complexity – From Defect Phase Diagrams to Material Properties, project ID 409476157. This project has received funding from the European Research Council (ERC) under the European Union's Horizon 2020 research and innovation programme (grant agreement No. 852096 FunBlocks). This work contains results obtained from experiments performed at the Ernst Ruska-Centre (ER-C) for Microscopy and Spectroscopy with Electrons at the Forschungszentrum Jülich (FZJ) in Germany. The ER-C beam-time access was provided via the Core Facility Project RWTH IMM SP2. The authors gratefully acknowledge the computing time provided to them at the NHR Center NHR4CES at RWTH Aachen University (project number p0020267). This is funded by the Federal Ministry of Education and Research, and the state governments participating on the basis of the resolutions of the GWK for national high performance computing at universities (www.nhr-verein.de/unsere-partner).

Appendix A. Supplementary data

Supplementary material related to this article can be found online at https://doi.org/10.1016/j.actamat.2025.121604.

Data availability

The data used in this publication was managed using the framework and metadata scheme provided by project A07 within SFB1394 Structural and Chemical Atomic Complexity — From Defect Phase Diagrams to Material Properties, project ID 409476157 funded by the Deutsche Forschungsgemeinschaft (DFG) and the research data management platform Coscine with storage space granted by the Research Data Storage (RDS) of the DFG and Ministry of Culture and Science of the State of North Rhine-Westphalia (DFG: INST222/1261-1 and MKW: 214-4.06.05.08 - 139057). The data that support the findings of this study are openly available on Zenodo at https://zenodo.org/records/17310990.

References

[1] M. Ashby, Materials–a brief history, Phil. Mag. Lett. 88 (9–10) (2008) 749–755.
[2] T.G. Akhmetshina, V.A. Blatov, D.M. Proserpio, A.P. Shevchenko, Topology of intermetallic structures: from statistics to rational design, Acc. Chem. Res. 51 (1) (2018) 21–30.
[3] A. Merchant, S. Batzner, S.S. Schoenholz, M. Aykol, G. Cheon, E.D. Cubuk, Scaling deep learning for materials discovery, Nature 624 (7990) (2023) 80–85.
[4] W. Luo, Z. Xie, P.-L. Sun, J.-L. Gibson, S. Korte-Kerzel, Plasticity of the Nb-rich μ-Co_7Nb_6 phase at room temperature and 600°C, Acta Mater. 246 (2023) 118720.
[5] W. Luo, Z. Xie, S. Zhang, J. Guénolé, P.-l. Sun, A. Meingast, A. Alhassan, X. Zhou, F. Stein, L. Pizzagalli, et al., Tailoring the plasticity of topologically close-packed phases via the crystals' fundamental building blocks, Adv. Mater. 35 (24) (2023) 2300586.
[6] W. Steurer, J. Dshemuchadse, Intermetallics: structures, properties, and statistics, vol. 26, Oxford University Press, 2016.
[7] P. Paufler, G. Schulze, Plastic deformation of the intermetallic compound $MgZn_2$, Phys. Status Solidi (B) 24 (1) (1967) 77–87.
[8] P. Paufler, G. Schulze, Gleitsysteme innermetallischer verbindungen, Krist. Tech. 2 (4) (1967) K11–K14.
[9] P. Paufler, J. Marschner, G. Schulze, The mobility of grown-in dislocations in the intermetallic compound $MgZn_2$ II. Stress dependence of basal slip at 390°C, Phys. Status Solidi (B) 43 (1) (1971) 279–282.
[10] T. Müller, H. Krahl, P. Paufler, A. Lamsa, G. Schulze, Gleitbanduntersuchungen während und nach verformung der intermetallischen verbindung $MgZn_2$, Krist. Tech. 7 (11) (1972) 1249–1264.
[11] H. Kubsch, P. Paufler, G. Schulze, The mobility of grown-in dislocations in the intermetallic compound $MgZn_2$ during prismatic slip, Phys. Status Solidi (A) 25 (1) (1974) 269–275.
[12] P. Paufler, Deformation-mechanism maps of the intermetallic compound $MgZn_2$, Krist. Tech. 13 (5) (1978) 587–590.
[13] P. Paufler, Early work on laves phases in east Germany, Intermetallics 19 (4) (2011) 599–612.
[14] M.F. Chisholm, S. Kumar, P. Hazzledine, Dislocations in complex materials, Science 307 (5710) (2005) 701–703.
[15] M. Kronberg, Plastic deformation of single crystals of sapphire: basal slip and twinning, Acta Metall. 5 (9) (1957) 507–524.
[16] K. Kishida, M. Okutani, H. Inui, Direct observation of zonal dislocation in complex materials by atomic-resolution scanning transmission electron microscopy, Acta Mater. 228 (2022) 117756.
[17] A. Mussi, A. Henzelmeier, T. Weidner, M. Novelli, Y. Wenbo, F. Cuvilly, T. Grosdidier, A. Guitton, Experimental evidence of zonal dislocations in the Ti_2AlC MAX phase, Mater. Charact. 200 (2023) 112882.
[18] M. Feuerbacher, M. Heggen, Metadislocations, Dislocations Solids 16 (2010) 109–170.
[19] M. Heggen, L. Houben, M. Feuerbacher, Plastic-deformation mechanism in complex solids, Nat. Mater. 9 (4) (2010) 332–336.
[20] S. Korte-Kerzel, V. Schnabel, W.J. Clegg, M. Heggen, Room temperature plasticity in m-$Al_{13}Co_4$ studied by microcompression and high resolution scanning transmission electron microscopy, Scr. Mater. 146 (2018) 327–330.
[21] P. Hazzledine, K. Kumar, D.B. Miracle, A. Jackson, Synchroshear of laves phases, MRS Online Proc. Libr. (OPL) 288 (1992) 591.
[22] P. Hazzledine, P. Pirouz, Synchroshear transformations in laves phases, Scr. Met. Mater. 28 (10) (1993) 1277–1282.
[23] O. Vedmedenko, F. Rösch, C. Elsässer, First-principles density functional theory study of phase transformations in $NbCr_2$ and $TaCr_2$, Acta Mater. 56 (18) (2008) 4984–4992.
[24] J. Guénolé, F.-Z. Mouhib, L. Huber, B. Grabowski, S. Korte-Kerzel, Basal slip in Laves phases: the synchroshear dislocation, Scr. Mater. 166 (2019) 134–138.
[25] Z. Xie, D. Chauraud, A. Atila, E. Bitzek, S. Korte-Kerzel, J. Guénolé, Unveiling the mechanisms of motion of synchro-Shockley dislocations in Laves phases, Phys. Rev. Mater. 7 (5) (2023) 053605.
[26] Z. Xie, D. Chauraud, A. Atila, E. Bitzek, S. Korte-Kerzel, J. Guénolé, Thermally activated nature of synchro-Shockley dislocations in Laves phases, Scr. Mater. 235 (2023) 115588.
[27] A.N. Ladines, R. Drautz, T. Hammerschmidt, Off-stoichiometric softening and polytypic transformations in the plastic deformation of the C14 Fe_2Nb Laves phase, Acta Mater. 260 (2023) 119326.
[28] T. Stollenwerk, N.Z.Z. Ulumuddin, P.-L. Sun, S.-H. Lee, M. Seehaus, K. Skokov, O. Gutfleisch, Z. Xie, S. Korte-Kerzel, Dislocation-mediated plasticity in the intermetallic $SmCo_5$ phase, Acta Mater. 266 (2024) 119669.
[29] M. Freund, D. Andre, P. Sun, C. Kusche, S. Sandlöbes-Haut, H. Springer, S. Korte-Kerzel, Plasticity of the C15-$CaAl_2$ Laves phase at room temperature, Mater. Des. 225 (2023) 111504.
[30] R. Peierls, The size of a dislocation, Proc. Phys. Soc. 52 (1) (1940) 34.
[31] S. Schröders, S. Sandlöbes, C. Birke, M. Loeck, L. Peters, C. Tromas, S. Korte-Kerzel, Room temperature deformation in the Fe_7Mo_6 μ-phase, Int. J. Plast. 108 (2018) 125–143.
[32] C. Zehnder, K. Czerwinski, K.D. Molodov, S. Sandlöbes-Haut, J.S.-L. Gibson, S. Korte-Kerzel, Plastic deformation of single crystalline C14 Mg_2Ca Laves phase at room temperature, Mat. Sci. Eng. A 759 (2019) 754–761.
[33] W. Luo, C. Kirchlechner, J. Zavašnik, W. Lu, G. Dehm, F. Stein, Crystal structure and composition dependence of mechanical properties of single-crystalline $NbCo_2$ Laves phase, Acta Mater. 184 (2020) 151–163.
[34] Y. Zhang, W. Zhang, B. Du, W. Li, L. Sheng, H. Ye, K. Du, Shuffle and glide mechanisms of prismatic dislocations in a hexagonal C14-type Laves-phase intermetallic compound, Phys. Rev. B 102 (13) (2020) 134117.
[35] Y. Cheng, G. Wang, J. Liu, L. He, Atomic configurations of planar defects in μ phase in Ni-based superalloys, Scr. Mater. 193 (2021) 27–32.
[36] W. Luo, C. Gasper, S. Zhang, P. Sun, N. Ulumuddin, A. Petrova, Y. Lysogorskiy, R. Drautz, Z. Xie, S. Korte-Kerzel, Non-basal plasticity in the μ-phase at room temperature, Acta Mater. 277 (2024) 120202.
[37] M. Freund, Z. Xie, P.-L. Sun, L. Berners, J. Spille, H. Wang, C. Thomas, M. Feuerbacher, M. Lipinska-Chwalek, J. Mayer, S. Korte-Kerzel, Influence of chemical composition on the room temperature plasticity of C15 Ca-Al-Mg Laves phases, Acta Mater. 276 (2024) 120124.
[38] D. Andre, M. Freund, U. Rehman, W. Delis, M. Felten, J. Nowak, C. Tian, M. Zubair, L. Tanure, L. Abdellaoui, et al., Metallographic preparation methods for the Mg based system Mg-Al-Ca and its Laves phases, Mater. Charact. 192 (2022) 112187.
[39] W.C. Oliver, G.M. Pharr, An improved technique for determining hardness and elastic modulus using load and displacement sensing indentation experiments, J. Mater. Res. 7 (6) (1992) 1564–1583.
[40] W.C. Oliver, G.M. Pharr, Measurement of hardness and elastic modulus by instrumented indentation: Advances in understanding and refinements to methodology, J. Mater. Res. 19 (1) (2004) 3–20.
[41] J.S.-L. Gibson, R. Pei, M. Heller, S. Medghalchi, W. Luo, S. Korte-Kerzel, Finding and characterising active slip systems: a short review and tutorial with automation tools, Materials 14 (2) (2021) 407.
[42] A. Kovács, R. Schierholz, K. Tillmann, FEI Titan G2 80-200 CREWLEY, JLSRF 2 (2016) A43–A43.
[43] A.P. Thompson, H.M. Aktulga, R. Berger, D.S. Bolintineanu, W.M. Brown, P.S. Crozier, P.J. In't Veld, A. Kohlmeyer, S.G. Moore, T.D. Nguyen, et al., LAMMPS-a flexible simulation tool for particle-based materials modeling at the atomic, meso, and continuum scales, Comput. Phys. Comm. 271 (2022) 108171.
[44] M. Poul, L. Huber, E. Bitzek, J. Neugebauer, Systematic atomic structure datasets for machine learning potentials: Application to defects in magnesium, Phys. Rev. B 107 (10) (2023) 104103.
[45] H.-S. Jang, D. Seol, B.-J. Lee, Modified embedded-atom method interatomic potentials for Mg–Al–Ca and Mg–Al–Zn ternary systems, J. Magnes. Alloy. 9 (1) (2021) 317–335.
[46] P. Hirel, Atomsk: A tool for manipulating and converting atomic data files, Comput. Phys. Comm. 197 (2015) 212–219.
[47] E. Bitzek, P. Koskinen, F. Gähler, M. Moseler, P. Gumbsch, Structural relaxation made simple, Phys. Rev. Lett. 97 (17) (2006) 170201.
[48] J. Guénolé, W.G. Nöhring, A. Vaid, F. Houllé, Z. Xie, A. Prakash, E. Bitzek, Assessment and optimization of the fast inertial relaxation engine (fire) for energy minimization in atomistic simulations and its implementation in lammps, Comput. Mater. Sci. 175 (2020) 109584.
[49] G. Henkelman, B.P. Uberuaga, H. Jónsson, A climbing image nudged elastic band method for finding saddle points and minimum energy paths, J. Chem. Phys. 113 (22) (2000) 9901–9904.
[50] G. Henkelman, H. Jónsson, Improved tangent estimate in the nudged elastic band method for finding minimum energy paths and saddle points, J. Chem. Phys. 113 (22) (2000) 9978–9985.
[51] D. Sheppard, R. Terrell, G. Henkelman, Optimization methods for finding minimum energy paths, J. Chem. Phys. 128 (13) (2008).
[52] Z. Xie, D. Chauraud, E. Bitzek, S. Korte-Kerzel, J. Guénolé, Laves phase crystal analysis (LaCA): Atomistic identification of lattice defects in C14 and C15 topologically close-packed phases, J. Mater. Res. 36 (10) (2021) 2010–2024.
[53] A. Stukowski, K. Albe, Extracting dislocations and non-dislocation crystal defects from atomistic simulation data, Modelling Simul. Mater. Sci. Eng. 18 (8) (2010) 085001.

[54] A. Stukowski, Visualization and analysis of atomistic simulation data with OVITO–the open visualization tool, Modelling Simul. Mater. Sci. Eng. 18 (1) (2009) 015012.
[55] P. Hirel, P. Cordier, P. Carrez, ⟨110⟩ {−110} edge dislocations in strontium titanate: Charged vs neutral, glide vs climb, Acta Mater. 285 (2025) 120636.
[56] Z. Zhan, M. Radovic, A. Srivastava, On the non-classical crystallographic slip in $Ti_{n+1}AlC_n$ MAX phases, Scr. Mater. 194 (2021) 113698.
[57] U.B. Asim, Z. Zhan, M. Radovic, A. Srivastava, Modeling the non-Schmid crystallographic slip in MAX phases, Int. J. Plast. 157 (2022) 103399.
[58] D. Caillard, J. Martin, et al., Thermally activated mechanisms in crystal plasticity, vol. 8, Amsterdam, 2003.
[59] M. Freund, D. Andre, C. Zehnder, H. Rempel, D. Gerber, M. Zubair, S. Sandlöbes-Haut, J.S.-L. Gibson, S. Korte-Kerzel, Plastic deformation of the $CaMg_2$ C14-Laves phase from 50-250 C, Materialia 20 (2021) 101237.
[60] A. Kanjilal, A. Ahmadian, M. Freund, P.-L. Sun, S. Korte-Kerzel, G. Dehm, J.P. Best, Temperature-driven nanoscale brittle-to-ductile transition of the C15 $CaAl_2$ Laves phase, Mater. Des. 244 (2024) 113206.
[61] M. Zubair, M. Felten, B. Hallstedt, M.V. Paredes, L. Abdellaoui, R.B. Villoro, M. Lipinska-Chwalek, N. Ayeb, H. Springer, J. Mayer, et al., Laves phases in Mg-Al-Ca alloys and their effect on mechanical properties, Mater. Des. 225 (2023) 111470.
[62] S. Medghalchi, M. Zubair, E. Karimi, S. Sandlöbes-Haut, U. Kerzel, S. Korte-Kerzel, Determination of the rate dependence of damage formation in metallic-intermetallic Mg-Al-Ca composites at elevated temperature using panoramic image analysis, Adv. Eng. Mater. 25 (21) (2023) 2300956.
[63] V.A. Yartys, M.V. Lototskyy, Laves type intermetallic compounds as hydrogen storage materials: a review, J. Alloys Compd. 916 (2022) 165219.
[64] L. Liang, F. Wang, M. Rong, Z. Wang, S. Yang, J. Wang, H. Zhou, et al., Recent advances on preparation method of Ti-based hydrogen storage alloy, J. Mater. Sci. Chem. Eng. 8 (12) (2020) 18.